Nanoscale

PAPER

View Article Online
View Journal | View Issue

Cite this: *Nanoscale*, 2017, **9**, 11765

Rapid, all dry microfabrication of three-dimensional Co_3O_4/Pt nanonetworks for high-performance microsupercapacitors†

Xinyu Ma,[a] Shuxuan Feng,[a] Liang He, *[a,b] Mengyu Yan,[a] Xiaocong Tian,[a] Yanxi Li,[c] Chunjuan Tang,[a,d] Xufeng Hong[a] and Liqiang Mai *[a,e]

Received 13th March 2017,
Accepted 12th July 2017

DOI: 10.1039/c7nr01789h

rsc.li/nanoscale

On-chip electrochemical energy storage devices have attracted growing attention due to the decreasing size of electronic devices. Various approaches have been applied for constructing the microsupercapacitors. However, the microfabrication of high-performance microsupercapacitors by conventional and fully compatible semiconductor microfabrication technologies is still a critical challenge. Herein, unique three-dimensional (3D) Co_3O_4 nanonetwork microelectrodes formed by the interconnection of Co_3O_4 nanosheets are constructed by controllable physical vapor deposition combined with rapid thermal annealing. This construction process is an all dry and rapid (≤5 minutes) procedure. Afterward, by sputtering highly electrically conductive Pt nanoparticles on the microelectrodes, the 3D Co_3O_4/Pt nanonetworks based microsupercapacitor is fabricated, showing a high volume capacitance (35.7 F cm^{-3}) at a scan rate of 20 mV s^{-1} due to the unique interconnected structures, high electrical conductivity and high surface area of the microelectrodes. This microfabrication process is also used to construct high-performance flexible microsupercapacitors, and it can be applied in the construction of wearable devices. The proposed strategy is completely compatible with the current semiconductor microfabrication and shows great potential in the applications of the large-scale integration of micro/nano and wearable devices.

Introduction

On-chip electrochemical energy storage devices (OEESDs), a kind of independent power supplies for portable electronic devices, wireless sensor networks and other self-powered microsystems, have attracted great attention due to their excellent electrochemical performance and miniaturized size.[1–7] Various OEESDs including microbatteries, microsupercapacitors (MSCs) and microscale hybrid devices made up of battery and capacitor materials with high energy/power density and long lifetime have been constructed recently.[8–11] The MSCs based on interdigital microelectrodes, a kind of OEESD, have been widely studied because of their high areal/volumetric utilization of active materials and short ion diffusion distance, contributing to their high electrochemical performance.[12–14]

Similar to traditional OEESDs,[15–21] most of the recently proposed devices are fabricated by various wet chemical processes, such as electrodeposition, chemical bath electrodeposition, drop-cast method and layer-by-layer assembly.[22–24] A great number of micro/nanostructures have been investigated for their applications in OEESDs, such as those of graphene based composites,[25–27] $Ni(OH)_2$,[28] MnO_2,[29,30] conductive polymers,[31–33] RuO_2,[34] *etc*. However, these wet chemical processes are usually less controllable, and the thickness of the microelectrode is non-uniform. The use of an aqueous solution would introduce various ions, which would result in unstable electrochemical performance of the devices.[35] In addition, the toxic waste water produced during the fabrication process causes environmental problems. Also, chemical vapor deposition (CVD) is a common kind of construction method.[36] Considering the inflammability and toxicity of the raw materials, sometimes CVD is dangerous and complicated. Recently, nanoporous carbon[37–39] based MSCs were constructed

[a]*State Key Laboratory of Advanced Technology for Materials Synthesis and Processing, International School of Materials Science and Engineering, Wuhan University of Technology, Wuhan 430070, Hubei, P. R. China. E-mail: hel@whut.edu.cn, mlq518@whut.edu.cn*
[b]*Department of Materials Science and NanoEngineering, Rice University, 6100 Main Street, Houston, TX 77005, USA*
[c]*Department of Materials Science and Engineering, Virginia Tech, Blacksburg, Virginia 24061, USA*
[d]*Department of Mathematics and Physics, Luoyang Institute of Science and Technology, Luoyang 471023, P. R. China*
[e]*Department of Chemistry, University of California-Berkeley, Berkeley, California 94702, USA*

†Electronic supplementary information (ESI) available. See DOI: 10.1039/c7nr01789h

by the pyrolysis of a photoresist. However, the construction process is always accompanied by a high pyrolysis temperature. Therefore, these methods are not fully suitable for the large-scale integration of nanomaterials into OEESDs since they are not fully compatible with the current semiconductor microfabrication technologies. In order to realize the mass production of OEESDs, it is important to develop a kind of microfabrication method which is completely compatible with modern micro/nanofabrication technologies. In addition, with the development of portable devices, wearable electronic devices have attracted a lot of attention in the past decade. Due to their high power density, flexible MSCs show their potential in applications of the power sources of wearable electronic devices. A method which can also help us construct flexible OEESDs will greatly extend its applications in the construction of wearable devices.

Among the electrode materials applied in supercapacitors, Co_3O_4 is particularly attractive by virtue of its great redox activity and high capacity as the cathode material of hybrid devices.[40] Distinctive capacitive characteristics of Co_3O_4 are also observed when it is used as the anode material of supercapacitors.[41] Most of the reported synthesis methods and integration approaches of Co_3O_4 nanostructures are complicated or require long-time annealing.[42–44] As a result, the Co_3O_4 nanomaterials are difficult to be integrated on the microscale current collectors which makes the applications of Co_3O_4 in MSCs a critical issue.

Herein, we proposed a facile, rapid and controllable approach utilizing rapid thermal annealing (RTA) to convert Co thin films into three-dimensional (3D) Co_3O_4 nanonetworks at a low temperature on a large scale, which are employed as the interdigital microelectrode of MSCs. The microfabrication process includes photolithography, physical vapor deposition (PVD) and RTA, which are the most common and useful procedures in the modern semiconductor industry. This construction process is an all dry process with a rapid (≤5 minutes (min)) annealing treatment. The 3D Co_3O_4 nanonetworks employed as the active material are constructed by the interconnection of individual Co_3O_4 nanosheets. A large number of nanopores form within the nanonetwork due to the overlap of nanosheets. Considering the poor electrical conductivity of Co_3O_4, 3D Co_3O_4/Pt nanonetworks MSC (Co_3O_4/Pt MSC) is further fabricated by a combination of Co_3O_4 with sputtered Pt nanoparticles (NPs), which can deliver electrons quickly; thus the electrochemical performance of MSC is improved. The Pt NPs in Co_3O_4/Pt MSC enhance the transportation of electrons between the Co_3O_4 nanosheets by an order of magnitude. The 3D interconnected nanonetwork and the inner porous structure promote the electron transport and ion diffusion, which result in the optimized electrochemical performance of the MSC.[45] As a result, the stack capacitance of Co_3O_4/Pt MSC reaches 35.7 F cm^{-3}, 1.5 times higher than that of Co_3O_4 MSC (22.3 F cm^{-3}). The microfabrication process is also used to construct the flexible MSC, showing similar electrochemical performance. Their excellent performance demonstrates that our strategy which is well compatible with the modern semiconductor industry provides a new design and approach for high-performance energy storage microdevices.

Experimental details

Microfabrication of on-chip Co_3O_4/Pt MSC

The microfabrication process of Co_3O_4/Pt MSC is illustrated in Fig. 1. A Si/SiO_2 wafer with a 300 nm thick SiO_2 or PI wafer was cleaned using an isopropyl alcohol solution for several minutes and utilized as the substrate on which the PR1-9000A photoresist (Futurrex, Inc. Co., Ltd) was uniformly spin-coated. Then the photolithography was followed to obtain the interdigital micropatterns of the photoresist. The PVD technique was utilized to deposit Cr/Au/Co layers (5/50/60 nm) on the surface of the sample in sequence and Pt NPs were deposited on the sample by magnetron sputtering (JEOL JFC-1600 Auto Fine Coater, power: 2 W and sputtering time: 40–240 s). Afterward

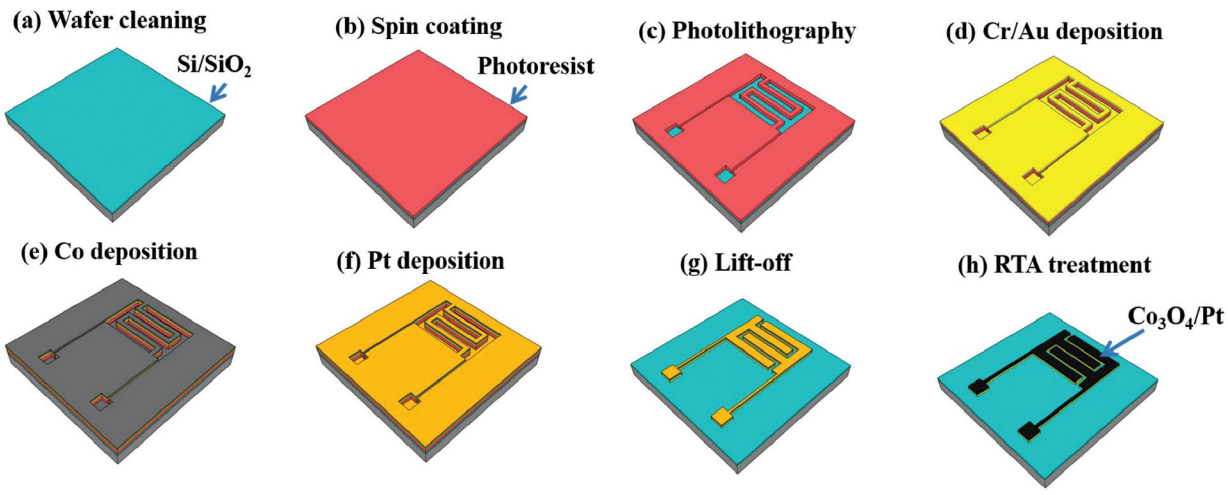

Fig. 1 Schematic illustration of the microfabrication process of the on-chip Co_3O_4/Pt MSC.

the lift-off process was conducted to remove the photoresist using acetone, and the patterned Cr/Au/Co/Pt microelectrodes were obtained. Finally, the Co_3O_4/Pt microelectrodes on the Cr/Au current collectors were fabricated by RTA at 350 °C for 5 min under an O_2 atmosphere. The efficient area of the MSC is ~0.1066 cm^2. 1 M KOH was used as the electrolyte. The on-chip MSC was assembled after the electrolyte was dropped onto the microelectrodes. A Co_3O_4 MSC without Pt NPs was also fabricated by the same procedures except for the sputtering of Pt NPs for comparison. The fabrication process of double-layer Co_3O_4/Pt MSC is shown in Fig. S13.† The PR1-9000A photoresist was uniformly spin-coated on the Co_3O_4/Pt MSC. Photolithography was utilized to obtain the interdigital micropatterns of the photoresist on the microelectrode of Co_3O_4/Pt MSC. The second Cr/Au/Co layer was deposited by PVD and Pt NPs were deposited by magnetron sputtering. Finally, the double-layer Co_3O_4/Pt MSC was obtained after annealing under an O_2 atmosphere for 5 minutes.

Characterization of the MSC

The thicknesses of on-chip Co_3O_4 MSC and Co_3O_4/Pt MSC were measured using a stylus surface profiler (Bruker Dektaker TX). Scanning electron microscopy (SEM) images were observed using a JEOL-7100F field-emission SEM at an acceleration voltage of 20 kV. Energy-dispersive X-ray spectra (EDS) were collected by an Oxford IE250 system. The crystallographic information of the as-fabricated microelectrodes was characterized using a Bruker D8 Discover X-ray diffractometer equipped with a Co-Kα radiation source (λ = 1.7902 Å). Transmission electron microscopy (TEM) images were collected using a Titan G2 60-300 Probe Cs Corrector HRSTEM. X-ray photoelectron spectroscopy (XPS) spectra were recorded using a VG Multilab 2000. Raman spectra were obtained using a Renishaw RM-1000 laser Raman microscopy system. All of the electrochemical tests were conducted using an Autolab PGSTAT302N. Electrical conductivity measurements were performed using a semiconductor device analyzer (Agilent, B1500A) and a probe station (Lake shore, PPT4).

Results and discussion

The digital photograph of the as-fabricated MSC is shown in Fig. 2a. The width of each interdigital microelectrode and the interspace of two microelectrodes are 400 and 100 μm, respectively. As shown in Fig. 2b, the Co film is uniformly deposited on the Cr/Au collector and no cracks are observed on its surface after the RTA treatment. The SEM images of the Co_3O_4/Pt microelectrode are shown in Fig. 2c; it can be found that the Co_3O_4 nanonetworks consist of Co_3O_4 nanosheets which are grown homogeneously on the Cr/Au current collectors on a large scale after annealing at 350 °C for 5 min. The length and width of the Co_3O_4/Pt nanosheets are about 100 and 5 nm, respectively. The nanoscale thickness of the interdigital microelectrode is 153.6 nm, which would increase the accessible surface area of the electrolyte. Furthermore, the nanonetwork

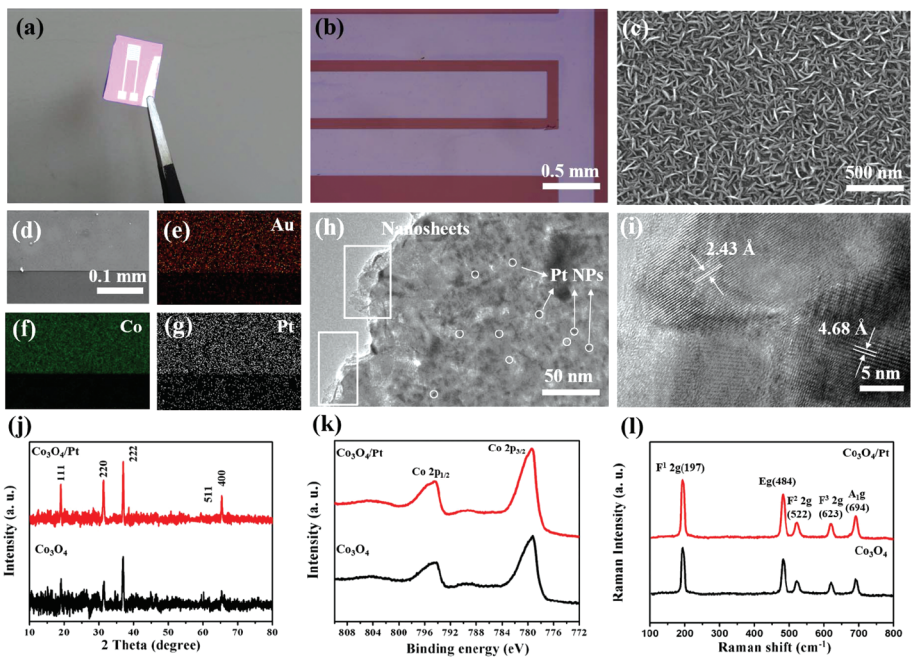

Fig. 2 Morphology, elemental composition and phase composition of planar MSCs. (a) Digital camera image of a Co_3O_4/Pt MSC. (b) Bright-field optical images of the Co_3O_4/Pt MSC. (c) FESEM image of Co_3O_4/Pt nanonetworks on the interdigital microelectrode. (d–g) SEM image and corresponding elemental mappings of Au, Co, and Pt of an interdigital microelectrode. (h) TEM image of the Co_3O_4/Pt microelectrode. (i) HRTEM image of Co_3O_4 in the Co_3O_4/Pt microelectrode. (j) XRD patterns of the Co_3O_4/Pt and Co_3O_4 microelectrodes. (k) XPS spectra of the Co 2p binding energy region of the Co_3O_4/Pt and Co_3O_4 microelectrodes. (l) Raman spectra of the Co_3O_4/Pt and Co_3O_4 microelectrodes.

structure can further enhance the electron conduction. Meanwhile, lots of nanopores in the inner space of the nanosheets could promote the penetration of the electrolyte and the ion diffusion. The corresponding elemental mappings of the selected area, with one interdigital microelectrode and its adjacent interspace of Co_3O_4/Pt MSC, are shown in Fig. 2d–g, and Fig. 2d is the SEM image of the selected area. A clear comparison between the interdigital microelectrode and the interspace indicates that the fine patterned microelectrode reserves its geometrical configuration after the RTA process. The distribution of Au, Co and Pt on the interdigital microelectrode is uniform. Pt NPs are located on an individual Co_3O_4 nanosheet. Thus, the aggregation of Pt NPs could be fully avoided. The interdigital microelectrode which consists of the Co_3O_4 nanonetwork and Pt NPs is observed in the TEM image (Fig. 2h). Pt NPs show a higher contrast owing to their high molecular weight in the dark-field TEM image (Fig. S1†). The high-resolution TEM (HRTEM) image (Fig. 2i) shows the lattice fringes with the lattice spacing of 2.43 and 4.68 Å, which correspond to the (311) and (111) crystal planes of Co_3O_4 (JCPDS No. 00-042-1467), respectively. The SEM and TEM images of the Co_3O_4 microelectrode without the sputtering of Pt NPs are shown in Fig. S2.† Similarly, the Co_3O_4 nanonetworks with lower density are homogeneously distributed on the current collector. Few Pt NPs have no influence on the growth of Co_3O_4 nanosheets during the RTA process. The (311) and (222) crystal planes of Co_3O_4 with the spacing of 2.43 and 2.32 Å are observed in the HRTEM image of the Co_3O_4 nanonetwork.[46] Temperature and annealing time of the RTA process as well as the sputtering time of Pt NPs pose important influence on the morphology of Co_3O_4/Pt microelectrodes. Fig. S3† shows the SEM images of the Co film with Pt NPs after annealing under an O_2 atmosphere at 450 °C for 5 min. However, the morphology of the film annealed at 450 °C for 5 min is non-uniform and the nanosheets are contorted due to the higher annealing temperature, decreasing the interface area of the nanostructures, which makes ion/electron immigration difficult. The nanonetwork cannot form due to the low growth density of Co_3O_4 nanosheets. Fig. S4† shows the morphology of the Co_3O_4/Pt microelectrode with longer Pt sputtering times of 160 and 240 s followed by the RTA treatment at 350 °C for 5 min. It is inferred that the thick Pt layer (Fig. S4b–d†) hinders the growth of Co_3O_4 nanosheets and impedes electrolyte penetration.

The phase of the active material obtained by the RTA process was characterized by X-ray diffraction (XRD). Fig. 2j shows the XRD patterns of Co_3O_4 and Co_3O_4/Pt microelectrodes after RTA at 350 °C for 5 min. By comparing these two patterns, the main diffraction peaks of the two samples are well indexed to the cubic Co_3O_4 phase (JCPDS No. 00-042-1467) with the space group of $Fd\bar{3}m$,[47] demonstrating that both samples have been oxidized into Co_3O_4 after a short annealing treatment at 350 °C for 5 min. No clear peaks of Pt can be observed due to its low content in the Co_3O_4/Pt microelectrode. Fig. 2k shows the XPS results of the Co_3O_4 and Co_3O_4/Pt microelectrodes, in which two elemental signals of Co and Pt are apparently observed. The XPS spectra of Co_3O_4 and Co_3O_4/Pt show two main peaks of Co $2p_{3/2}$ and Co $2p_{1/2}$ at the binding energies of 779.3 and 794.3 eV with a spin energy separation of 15 eV, together with two satellite peaks, corresponding to the characteristic peaks of Co_3O_4.[48] Besides, the peak of Pt $4f_{7/2}$ is also captured in the XPS spectrum of Co_3O_4/Pt (Fig. S5†), which can further confirm the existence of Pt in the Co_3O_4/Pt microelectrode. Based on the XPS spectrum, the content of Pt in Co_3O_4/Pt is calculated to be ~2.8%. The low content of Pt NPs does not increase the cost of the MSC obviously. The Raman spectra of Co_3O_4 and Co_3O_4/Pt microelectrodes are shown in Fig. 2l. Both of the microelectrodes have the same peaks at 198, 484, 522, 622 and 694 cm^{-1}, corresponding to the F^1_{2g}, E_g, F^2_{2g}, F^3_{2g} and A_{1g} modes of crystalline Co_3O_4, respectively.[44] This result demonstrates that Pt NPs sputtered on the surface of the Co film have no influence on the composition and structure of the active material, and Pt NPs are still retained in the initial metal state. All the characterization studies conducted above confirmed that the active electrode is the Co_3O_4 nanonetworks and highly electrically conductive Pt NPs deposited on the Co_3O_4 nanonetworks.

The electrochemical behaviors of the Co_3O_4/Pt MSC using a 1 M KOH electrolyte were evaluated using two-electrodes with symmetrical Co_3O_4/Pt or Co_3O_4 microelectrodes as cathode and anode. The potential window ranged from 0 to 0.8 V. Cyclic voltammetry (CV) curves measured at various scan rates varying from 20 to 10 000 mV s^{-1} are presented in Fig. 3a and b. To accurately identify the intrinsic properties of MSCs, stack capacitance (C, in F cm^{-3}), energy density (E, in Wh cm^{-3}) and power density (P, in W cm^{-3}) are calculated using the equations from a previous study.[49]

It is apparent that the shapes of the CV curves in Fig. 3a are quasi-rectangular at a low scan rate, which indicates that the faradaic reactions exist during the charge and discharge processes. The faradaic reactions accompanied by the reversible transformation between Co^{2+} and Co^{4+} are observed using a three-electrode test system (Fig. S6a†). The negative electrode shows capacitance characteristics due to the high surface area of the Co_3O_4 nanosheets (Fig. S6b†). The quick redox reaction increases the capacitance of the whole device.[50] Meanwhile, the shapes of the CV curves still remain rectangular at a high scan rate of 2000–10 000 mV s^{-1}, as shown in Fig. 3b. It is demonstrated that the Co_3O_4/Pt microelectrodes show excellent ion/electron conduction. At a low scan rate of 20 mV s^{-1}, the energy density of the Co_3O_4/Pt MSC is 3.17 mWh cm^{-3} and its stack capacitance is 31.7 F cm^{-3} which is superior to those of Co_3O_4 MSC (22.3 F cm^{-3}) and some recently reported values of transition metal oxide-based MSCs (17.4 F cm^{-3} for a CoO nanoflower-based MSC[51] and 11.57 F cm^{-3} for an rGO/Fe_2O_3-based MSC[52]). The specific stack capacitance of Co_3O_4/Pt MSC remains 2.96 F cm^{-3} with a high stack power density of 47.4 W cm^{-3} at an ultrahigh scan rate of 10 000 mV s^{-1}. The CV test of the Co_3O_4 MSC was conducted as well, the result of which is shown in Fig. S7a and b.† The shapes of the CV curves of the Co_3O_4 MSC are nearly rectangular which further confirms its similar electrochemical performance to that of

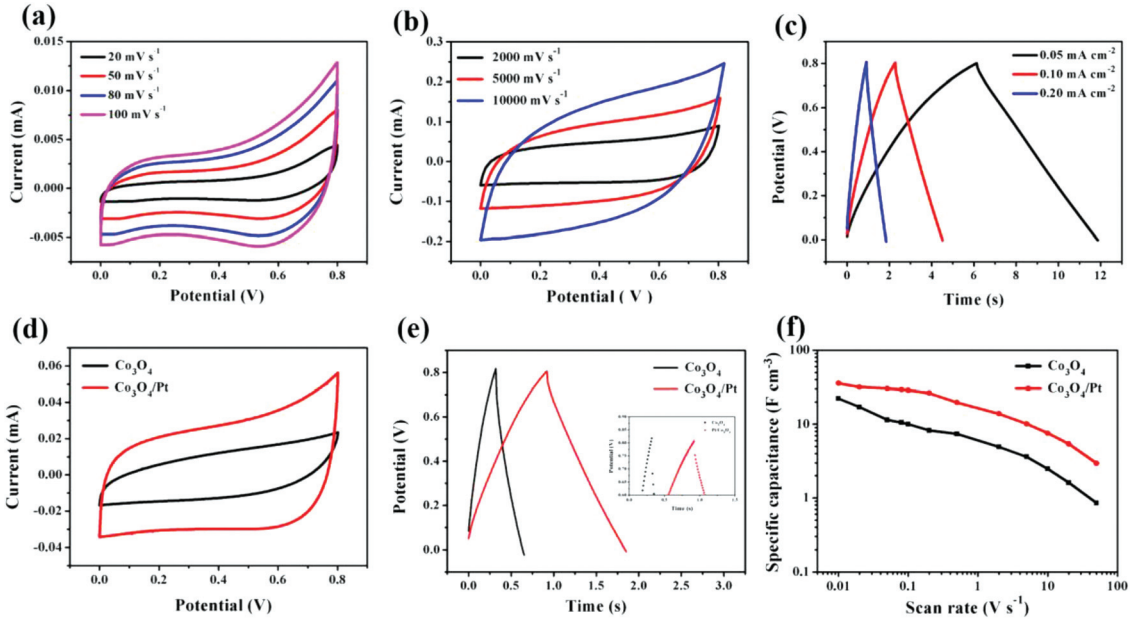

Fig. 3 Electrochemical performance of planar Co_3O_4/Pt and Co_3O_4 MSCs. (a, b) CV curves of the Co_3O_4/Pt MSC at different scan rates in 1 M KOH with a potential window from 0 to 0.8 V. (c) Galvanostatic charge–discharge curves of the Co_3O_4/Pt MSC at various current densities. (d) CV curves of the Co_3O_4/Pt and Co_3O_4 MSCs at the scan rate of 1 V s^{-1}. (e) Galvanostatic charge–discharge curves of Co_3O_4/Pt and Co_3O_4 MSCs at a current density of 0.2 mA cm^{-2}. The inset in (e) represents the initial voltage drop of the Co_3O_4/Pt and Co_3O_4 MSCs. (f) Evolution of the stack capacitance of the Co_3O_4/Pt and Co_3O_4 MSCs at different scan rates.

Co_3O_4/Pt. However the response current of the Co_3O_4 MSC at the same scan rate is much less than that of Co_3O_4/Pt MSC, corresponding to a lower capacitance.

The galvanostatic charge–discharge curves of the Co_3O_4/Pt MSC under different current densities (from 50 to 200 μA cm^{-2}) are presented in Fig. 3c. Both charge and discharge curves display relatively symmetric triangular shapes. The stack capacitance of the Co_3O_4/Pt MSC is calculated using the equation from a previous study.[49] At the current density of 0.5 mA cm^{-2}, the capacitance of Co_3O_4/Pt MSC is 25.0 F cm^{-3} with a coulombic efficiency (CE) of 93.1%. The capacitance of the Co_3O_4/Pt MSC remains 15.0 F cm^{-3} with a CE approaching 100% at the current density of 2 mA cm^{-2}. Furthermore, the same evaluation was also conducted for the Co_3O_4 MSC, the result of which is shown in Fig. S7c and d.† The discharge time of the Co_3O_4 MSC is shorter than that of the Co_3O_4/Pt MSC, showing a lower capacitance which is due to the lower electrical conductivity.

To investigate the effect of Pt NPs clearly, the CV curves of Co_3O_4 and Co_3O_4/Pt MSCs at the same scan rate of 1 V s^{-1} are shown in Fig. 3d; it is apparent that the CV curve of the Co_3O_4/Pt MSC is 2.91 times bigger than that of the Co_3O_4 MSC, indicating a higher capacitance of the Co_3O_4/Pt MSC. Similarly, the galvanostatic charge–discharge curve in Fig. 3e apparently indicates that the Co_3O_4/Pt MSC has a higher capacitance at a high current density of 200 μA cm^{-2}. The volume capacitance increases from 4.29 to 12.10 F cm^{-3} after the sputtering of Pt NPs. In addition, the initial voltage drop of the Co_3O_4/Pt MSC decreases from 0.135 to 0.053 V, showing its lower internal resistance. The specific capacitances of the Co_3O_4/Pt and Co_3O_4 MSCs which were calculated from their CV curves are shown in Fig. 3f. After the sputtering of Pt NPs, the capacitance and rate performance of the Co_3O_4/Pt MSC improved remarkably compared with those of the Co_3O_4 MSC, especially at 50 V s^{-1}, where the capacitance of the Co_3O_4/Pt MSC is 3.48 times higher than that of the Co_3O_4 MSC.

The bare Pt microelectrode based MSC is also fabricated and its symmetrical two-electrode CV behavior is evaluated in Fig. S8.† Comparing the current of the bare Pt microelectrode based MSC with that of the Co_3O_4/Pt MSC at the same scan rate, it is clear that pure Pt and the current collector make little contribution to the stack capacitance. It is indicated that Co_3O_4 plays a main role in the capacitance of the MSC. Also, different sputtering times of Pt have a nonnegligible effect on the electrochemical performance of the Co_3O_4/Pt MSC. The areal specific capacitances of MSCs with different sputtering times of Pt NPs at the scan rate of 20 mV s^{-1} are shown in Fig. S9,† which demonstrate that the electrochemical performance of the Co_3O_4/Pt MSC with a Pt sputtering time of 80 s is the best. A thicker layer of Pt with a sputtering time of 160–240 s hinders the oxidation of the cobalt film, resulting in a lower capacitance.

Fig. 4a shows the cycling performance of the Co_3O_4/Pt and Co_3O_4 MSCs after 5000 cycles at a scan rate of 2000 mV s^{-1}. The Co_3O_4/Pt MSC shows better cycling stability with a capacitance retention of 91.9% after 5000 cycles. In contrast, the capacitance of the Co_3O_4 MSC shows extreme decreases after 1500 cycles, and barely retains 49.2% of the initial value

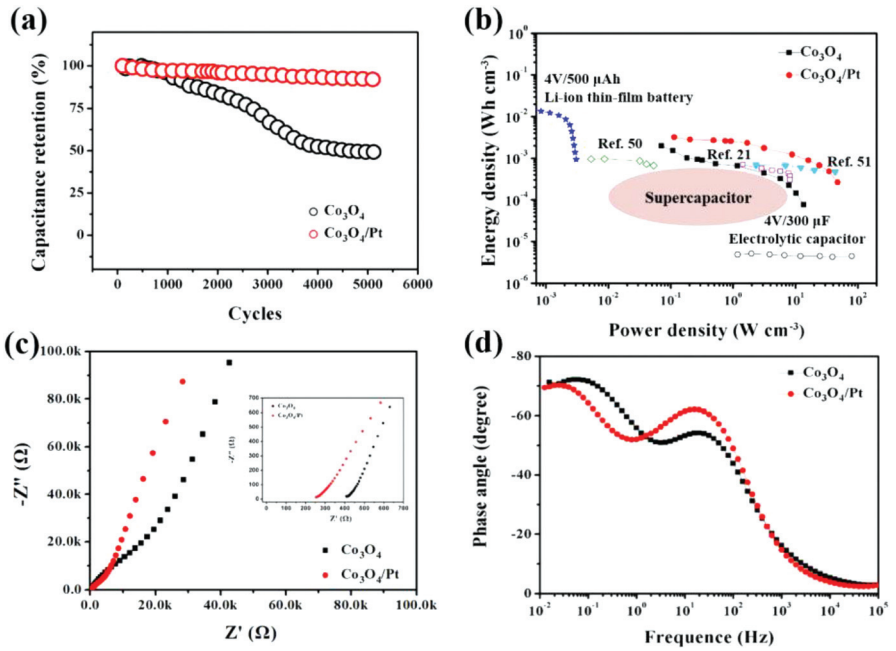

Fig. 4 Cycling performance, Ragone plots and EIS curves of planar MSCs. (a) Cycling performance (normalized) of the Co_3O_4/Pt and Co_3O_4 MSCs at the scan rate of 2 V s^{-1} over 5000 cycles. (b) Ragone plots of volumetric specific energy and power densities of Co_3O_4/Pt MSC, Co_3O_4 MSC, Li-ion thin film battery, other reported MSCs and electrolytic capacitors. (Thicknesses of $K_2Co_3(P_2O_7)_2{\cdot}2H_2O$ nanocrystal whiskers, PANI and reduced graphene/carbon nanotube are 1.2 μm, 0.9 μm and 6 μm, respectively.) (c) Nyquist plots of the Co_3O_4/Pt and Co_3O_4 MSCs. The inset shows the high-frequency region. (d) Bode plot of the impedance of Co_3O_4/Pt and Co_3O_4 MSCs.

after 5000 cycles, which can be ascribed to its low electrical conductivity, whereas the MSC integrated with Pt NPs, which strengthen the ionic accessibility and diffusion and increase the surface area of the electrochemically active material, exhibits stable cycling performance. The Ragone plots of the energy density and the power density of Co_3O_4/Pt and Co_3O_4 MSCs are shown in Fig. 4b. At all scan rates, higher energy density and power density of the Co_3O_4/Pt MSC show its better electrochemical performance, especially at a higher scan rate. The energy density of the Co_3O_4/Pt MSC is comparable with that of lithium ion film batteries, and it shows much higher power density. Notably, the Co_3O_4/Pt MSC also shows a higher energy density than those of supercapacitors, electrolytic capacitors and other MSCs with $K_2Co_3(P_2O_7)_2{\cdot}2H_2O$ nanocrystal whiskers,[53] polyaniline[22] and reduced graphene/carbon nanotubes[54] at comparable power densities.[49] It is indicated that the Co_3O_4/Pt MSC shows great potential in applications for high-performance micro-energy storage devices/systems.

It is inferred that the great improvement of the Co_3O_4/Pt MSC in electrochemical performance can be ascribed to the fact that Pt NPs sputtered on the surface of Co_3O_4 accelerate the electron migration process during the charge and discharge processes. As shown in Fig. S10,† current–voltage tests of one finger of both the Co_3O_4/Pt and Co_3O_4 microelectrodes are conducted. The current of the Co_3O_4/Pt MSC increases by almost 1 order of magnitude compared to that of the Co_3O_4 MSC at a bias voltage of 1 V, presenting a much higher conductivity of Co_3O_4/Pt. In addition, the increased specific surface area of the microelectrodes would account for the improvement in their performance as well. To further confirm this assumption, we investigated the electronic double layer capacitance (EDLC) of the Co_3O_4/Pt and Co_3O_4 microelectrodes (Fig. S11†), which can be used to estimate the magnitude of the electroactive electrode's surface. The Co_3O_4/Pt MSC shows a much higher current density of 3.91 μA cm^{-2}, which is two times higher than that of the Co_3O_4 MSC at the scan rate of 5–20 mV s^{-1}.

The Co_3O_4/Pt MSC shows an enhanced EDLC, indicating the increased specific surface area of the Co_3O_4/Pt microelectrodes. This is consistent with the SEM images which show that the growth density of Co_3O_4/Pt nanosheets is higher than that of pristine Co_3O_4 nanosheets (Fig. 2c and Fig. S2a†).

The electrochemical impedance spectroscopy (EIS) results of the Co_3O_4/Pt and Co_3O_4 MSCs in the range of 100 kHz to 0.01 Hz are shown in Fig. 4c. The Co_3O_4/Pt MSC shows a lower equivalent series resistance (ESR) compared with the Co_3O_4 MSC. The small ESR is ascribed to the following reasons: (a) high electrical conductivity of Co_3O_4/Pt after the sputtering of Pt NPs on the Co_3O_4 nanonetworks; (b) high contact area between the electrolyte and the electrode; (c) enhanced electron conduction due to the unique 3D interconnected network structure; (d) short ion diffusion distance after the electrolyte infiltrates into nanopores. In the region of medium frequency, the much shorter Warburg region of the plot, which reflects the frequency dependence of the electrolyte ions' diffusion into

the Co_3O_4/Pt microelectrodes, indicates that the ion diffusion of Co_3O_4 is enhanced. A comparison of the high frequencies of the EIS curves shows that the Co_3O_4/Pt MSC is more like an ideal capacitor than the Co_3O_4 MSC due to its more vertical line.[55] Also, the dependence of the phase angle on the frequency of the MSCs is shown in Fig. 4d. The RC time constant (τ_0 = 7.9 ms) of the Co_3O_4/Pt MSC is shorter than that of the Co_3O_4 MSC (τ_0 = 12.9 ms). It is indicated that the Co_3O_4/Pt MSC can provide excellent power response.[9]

By virtue of the rapid construction process, the PI substrate also can be annealed using a quick annealing oven. The digital image and the electrochemical performance of the Co_3O_4/Pt MSC are shown in Fig. S12.† The flexible Co_3O_4/Pt MSC shows similar CV and galvanostatic charge–discharge curves to those of the Co_3O_4/Pt MSC on the Si/SiO_2 substrate. The capacitance of the flexible Co_3O_4/Pt MSC is 23.05 F cm^{-3} at a scan rate of 0.02 V s^{-1} and remains at 6.27 F cm^{-3} at a high scan rate of 10 V s^{-1}. The equivalent series impedance of the flexible Co_3O_4/Pt MSC is not so much different from that of the Co_3O_4/Pt MSC on the Si/SiO_2 substrate. The above results illustrate that the construction process is also suitable for fabricating the flexible energy storage devices.

The vertical stacked electrode configuration is used to increase the areal capacitance of the whole device.[56] The CV and charge–discharge curves of the double-layer Co_3O_4/Pt MSC are similar to those of the single-layer Co_3O_4/Pt MSC (Fig. S14a–d†). However the areal capacitance of the double-layer Co_3O_4/Pt MSC increases from 0.49 mF cm^{-2} to 0.93 mF cm^{-2} at the scan rate of 20 mV s^{-1} (Fig. S14e†). The charge–discharge time of the double-layer Co_3O_4/Pt MSC is 10.51 s at the current density of 0.05 mA cm^{-2}, which is much higher than that of the single-layer Co_3O_4/Pt MSC (Fig. S14f†).

Conclusions

In summary, a MSC with 3D Co_3O_4 nanonetworks decorated with Pt NPs was fabricated by PVD combined with RTA. Many advantages including rapid microfabrication (<5 min), low cost and all dry process (avoiding potential ion contamination) are associated with the microfabrication process of the Co_3O_4/Pt MSC. Through constructing the 3D interconnected nanonetwork structure and sputtering of highly electrically conductive Pt, the capacitance of the Co_3O_4/Pt MSC is almost 1.5 times higher than that of the pristine Co_3O_4 MSC at a low scan rate, and increases to 3 times at a high scan rate (10 V s^{-1}). The capacitance fading rate after 5000 cycles also decreases from 59.8% to 8.9% after the deposition of Pt NPs. Based on the above advantages, this microfabrication process is fairly facile, and lends itself to mass production easily. Furthermore, other kinds of metals and high conductivity materials are also extremely promising to be applied and integrated into microdevices/systems by this highly productive microfabrication process, which will promote the development of micro electrochemical energy storage devices and other electronic microdevices.

Acknowledgements

This work was supported by the National Key Research and Development Program of China (2016YFA0202603 and 2016YFA0202604), the National Basic Research Program of China (2013CB934103), the Programme of Introducing Talents of Discipline to Universities (B17034), the National Natural Science Foundation of China (51521001, 51502227, and 51579198), the National Natural Science Fund for Distinguished Young Scholars (51425204), the China Postdoctoral Science Foundation (2015T80845), the Hubei Province Natural Science Fund (2016CFB582), Wuhan Morning Light Plan of Youth Science and Technology (No. 2017050304010316) and the Fundamental Research Funds for the Central Universities (WUT: 2016III001 and 2016III005). Prof. Liang He and Prof. Liqiang Mai gratefully acknowledge the financial support from the China Scholarship Council (No. 201606955094 and 201606955096).

Notes and references

1 J. Chmiola, C. Largeot, P.-L. Taberna, P. Simon and Y. Gogotsi, *Science*, 2010, **328**, 480–483.
2 M. Beidaghi and Y. Gogotsi, *Energy Environ. Sci.*, 2014, **7**, 867–884.
3 W. Gao, N. Singh, L. Song, Z. Liu, A. L. M. Reddy, L. Ci, R. Vajtai, Q. Zhang, B. Wei and P. M. Ajayan, *Nat. Nanotechnol.*, 2011, **6**, 496–500.
4 H. Hu, Z. Pei and C. Ye, *Energy Storage Mater.*, 2015, **1**, 82–102.
5 J. Wan, W. Bao, Y. Liu, J. Dai, F. Shen, L. Zhou, X. Cai, D. Urban, Y. Li, K. Jungjohann, M. S. Fuhrer and L. Hu, *Adv. Energy Mater.*, 2015, **5**, 1401742.
6 S. D. Lacey, J. Wan, A. v. W. Cresce, S. M. Russell, J. Dai, W. Bao, K. Xu and L. Hu, *Nano Lett.*, 2015, **15**, 1018–1024.
7 X. Xiao, T. Li, P. Yang, Y. Gao, H. Jin, W. Ni, W. Zhan, X. Zhang, Y. Cao, J. Zhong, L. Gong, W.-C. Yen, W. Mai, J. Chen, K. Huo, Y.-L. Chueh, Z. L. Wang and J. Zhou, *ACS Nano*, 2012, **6**, 9200–9206.
8 D. Pech, M. Brunet, H. Durou, P. Huang, V. Mochalin, Y. Gogotsi, P.-L. Taberna and P. Simon, *Nat. Nanotechnol.*, 2010, **5**, 651–654.
9 X. Tian, M. Shi, X. Xu, M. Yan, L. Xu, A. Minhas-Khan, C. Han, L. He and L. Mai, *Adv. Mater.*, 2015, **27**, 7476–7482.
10 C. Yin, L. He, Y. Wang, Z. Liu, G. Zhang, K. Zhao, C. Tang, M. Yan, Y. Han and L. Mai, *RSC Adv.*, 2016, **6**, 43436–43441.
11 H. Li, L. Peng, Y. Zhu, X. Zhang and G. Yu, *Nano Lett.*, 2016, **16**, 5938–5943.
12 M. F. El-Kady and R. B. Kaner, *Nat. Commun.*, 2013, **4**, 1475.
13 P. Huang, C. Lethien, S. Pinaud, K. Brousse, R. Laloo, V. Turq, M. Respaud, A. Demortière, B. Daffos, P. L. Taberna, B. Chaudret, Y. Gogotsi and P. Simon, *Science*, 2016, **351**, 691–695.

14 L. Mai, X. Tian, X. Xu, L. Chang and L. Xu, *Chem. Rev.*, 2014, **114**, 11828–11862.
15 Z. Niu, W. Zhou, X. Chen, J. Chen and S. Xie, *Adv. Mater.*, 2015, **27**, 6002–6008.
16 R. Liu, L. Wan, S. Liu, L. Pan, D. Wu and D. Zhao, *Adv. Funct. Mater.*, 2015, **25**, 526–533.
17 Q. Shi, R. Zhang, Y. Lv, Y. Deng, A. A. Elzatahrya and D. Zhao, *Carbon*, 2015, **84**, 335–346.
18 M. Yu, Z. Wang, Y. Han, Y. Tong, X. Lu and S. Yang, *J. Mater. Chem. A*, 2016, **4**, 4634–4658.
19 Y. Zeng, Y. Han, Y. Zhao, Y. Zeng, M. Yu, Y. Liu, H. Tang, Y. Tong and X. Lu, *Adv. Energy Mater.*, 2015, **5**, 1402176.
20 H. Xu, X. Hu, H. Yang, Y. Sun, C. Hu and Y. Huang, *Adv. Energy Mater.*, 2015, **5**, 1401882.
21 X. Xiao, C. Zhang, S. Lin, L. Huang, Z. Hu, Y. Cheng, T. Li, W. Qiao, D. Long, Y. Huang, L. Mai, Y. Gogotsi and J. Zhou, *Energy Storage Mater.*, 2015, **1**, 1–8.
22 C. Meng, J. Maeng, S. W. M. John and P. P. Irazoqui, *Adv. Energy Mater.*, 2014, **4**, 1301269.
23 B. Song, L. Li, Z. Lin, Z.-K. Wu, K.-s. Moon and C.-P. Wong, *Nano Energy*, 2015, **16**, 470–478.
24 Z.-S. Wu, K. Parvez, A. Winter, H. Vieker, X. Liu, S. Han, A. Turchanin, X. Feng and K. Müllen, *Adv. Mater.*, 2014, **26**, 4552–4558.
25 R. Z. Li, R. Peng, K. D. Kihm, S. Bai, D. Bridges, U. Tumuluri, Z. Wu, T. Zhang, G. Compagnini, Z. Feng and A. Hu, *Energy Environ. Sci.*, 2016, **9**, 1458–1467.
26 L. Liu, Z. Niu and J. Chen, *Chem. Soc. Rev.*, 2016, **45**, 4340–4363.
27 L. Peng, Y. Zhu, H. Li and G. Yu, *Small*, 2016, **12**, 6183–6199.
28 N. Kurra, N. A. Alhebshi and H. N. Alshareef, *Adv. Energy Mater.*, 2015, **5**, 1401303.
29 J. Han, Y.-C. Lin, L. Chen, Y.-C. Tsai, Y. Ito, X. Guo, A. Hirata, T. Fujita, M. Esashi, T. Gessner and M. Chen, *Adv. Sci.*, 2015, **2**, 1500067.
30 I. Nam, G.-P. Kim, S. Park, J. Park, N. D. Kim and J. Yi, *Nanoscale*, 2012, **4**, 7350–7353.
31 N. Kurra, M. K. Hota and H. N. Alshareef, *Nano Energy*, 2015, **13**, 500–508.
32 Z.-S. Wu, K. Parvez, S. Li, S. Yang, Z. Liu, S. Liu, X. Feng and K. Müllen, *Adv. Mater.*, 2015, **27**, 4054–4061.
33 Y. Shi and G. Yu, *Chem. Mater.*, 2016, **28**, 2466–2477.
34 J. Y. Hwang, M. F. El-Kady, Y. Wang, L. Wang, Y. Shao, K. Marsh, J. M. Ko and R. B. Kaner, *Nano Energy*, 2015, **18**, 57–70.
35 C. Weidlich, K. M. Mangold and K. Jüttner, *Electrochim. Acta*, 2005, **50**, 1547–1552.
36 J. Lin, C. Zhang, Z. Yan, Y. Zhu, Z. Peng, R. H. Hauge, D. Natelson and J. M. Tour, *Nano Lett.*, 2013, **13**, 72–78.
37 Y. Yang, L. He, C. Tang, P. Hu, X. Hong, M. Yan, Y. Dong, X. Tian, Q. Wei and L. Mai, *Nano Res.*, 2016, **9**, 2510–2519.
38 B. Hsia, M. S. Kim, M. Vincent, C. Carraro and R. Maboudian, *Carbon*, 2013, **57**, 395–400.
39 W. Li, J. Liu and D. Zhao, *Nat. Rev. Mater.*, 2016, **1**, 16023.
40 Q. Liao, N. Li, S. Jin, G. Yang and C. Wang, *ACS Nano*, 2015, **9**, 5310–5317.
41 J. S. Lee, D. H. Shin and J. Jang, *Energy Environ. Sci.*, 2015, **8**, 3030–3039.
42 T. Yu, Y. W. Zhu, X. J. Xu, Z. X. Shen, P. Chen, C. T. Lim, J. T. L. Thong and C. H. Sow, *Adv. Mater.*, 2005, **17**, 1595–1599.
43 Z. Qiao, D. Xu, F. Nie, G. Yang and K. Zhang, *J. Appl. Phys.*, 2012, **112**, 014310.
44 L. He, Z. Li and Z. Zhang, *Nanotechnology*, 2008, **19**, 155606.
45 Q. An, Q. Wei, P. Zhang, J. Sheng, K. M. Hercule, F. Lv, Q. Wang, X. Wei and L. Mai, *Small*, 2015, **11**, 2654–2660.
46 H. Liang, J. M. Raitano, L. Zhang and S.-W. Chan, *Chem. Commun.*, 2009, 7569–7571.
47 D. Cao, J. Chao, L. Sun and G. Wang, *J. Power Sources*, 2008, **179**, 87–91.
48 J. Cui, X. Zhang, L. Tong, J. Luo, Y. Wang, Y. Zhang, K. Xie and Y. Wu, *J. Mater. Chem. A*, 2015, **3**, 10425–10431.
49 X. Tian, B. Xiao, X. Xu, L. Xu, Z. Liu, Z. Wang, M. Yan, Q. Wei and L. Mai, *Nano Res.*, 2016, **9**, 1012–1021.
50 X. Xia, J. Tu, Y. Mai, X. Wang, C. Gu and X. Zhao, *J. Mater. Chem.*, 2011, **21**, 9319–9325.
51 Y. G. Zhu, Y. Wang, Y. Shi, J. I. Wong and H. Y. Yang, *Nano Energy*, 2014, **3**, 46–54.
52 S. Gu, Z. Lou, L. Li, Z. Chen, X. Ma and G. Shen, *Nano Res.*, 2016, **9**, 424–434.
53 H. Pang, Y. Zhang, W.-Y. Lai, Z. Hu and W. Huang, *Nano Energy*, 2015, **15**, 303–312.
54 M. Beidaghi and C. Wang, *Adv. Funct. Mater.*, 2012, **22**, 4501–4510.
55 Y. Sun, Q. Wu and G. Shi, *Phys. Chem. Chem. Phys.*, 2011, **13**, 17249–17254.
56 H. Hu, Z. Pei, H. Fan and C. Ye, *Small*, 2016, **12**, 3059–3069.

